**Article**

# Noninvasive Imaging and Correlative Histology of Cone Photoreceptor Structure in the Pig Retina

**Alison L. Huckenpahler[1], Joseph Carroll[1,2], Alexander E. Salmon[1], Benjamin S. Sajdak[1], Rebecca R. Mastey[2], Kenneth P. Allen[3,4], Henry J. Kaplan[5], and Maureen A. McCall[5,6]**

[1] Department of Cell Biology, Neurobiology & Anatomy, Medical College of Wisconsin, Milwaukee, WI, USA
[2] Department of Ophthalmology & Visual Sciences, Medical College of Wisconsin, Milwaukee, WI, USA
[3] Biomedical Resource Center, Medical College of Wisconsin, Milwaukee, WI, USA
[4] Department of Microbiology & Immunology, Medical College of Wisconsin, Milwaukee, WI, USA
[5] Department of Ophthalmology and Visual Sciences, University of Louisville, Louisville, KY, USA
[6] Department of Anatomical Sciences and Neurobiology, University of Louisville, Louisville, KY, USA

**Correspondence:** Maureen McCall, University of Louisville, School of Medicine, Department of Ophthalmology and Visual Sciences, 301 E. Muhammad Ali Blvd., Louisville, KY 40202, USA. e-mail: maureen.mccall@louisville.edu
Henry Kaplan, University of Louisville, School of Medicine, Department of Ophthalmology and Visual Sciences, 301 E. Muhammad Ali Blvd., Louisville, KY 40202, USA. e-mail: hank.kaplan@louisville.edu

**Purpose:** To evaluate different methods of studying cone photoreceptor structure in wild-type (WT) and transgenic pigs carrying the human rhodopsin P23H mutant gene (TgP23H).

**Methods:** For in vivo imaging, pigs were anesthetized with tiletamine-zolazepam and isoflurane and given lidocaine-bupivacaine retrobulbar injections. Stay sutures and a custom head mount were used to hold and steer the head for adaptive optics scanning light ophthalmoscopy (AOSLO). Six WT and TgP23H littermates were imaged at postnatal day 30 (P30), P90, and P180 with AOSLO and optical coherence tomography (OCT), and two additional sets of littermates were imaged at P3 and P15 with OCT only. AOSLO imaging and correlative differential interference contrast microscopy were performed on a P240 WT pig and on WT and TgP23H littermates at P30 and P180.

**Results:** AOSLO cone density generally underestimates histology density (mean difference $\pm$ SD = 24.8% $\pm$ 21.4%). The intensity of the outer retinal hyperreflective OCT band attributed to photoreceptors is attenuated in TgP23H pigs at all ages. In contrast, AOSLO images show cones that retain inner and outer segments through P180. At retinal locations outside the visual streak, TgP23H pigs show a heterogeneous degenerating cone mosaic by using two criteria: variable contrast on a split detector AOSLO and high reflectivity on a confocal AOSLO.

**Conclusions:** AOSLO reveals that the cone mosaic is similar to ex vivo histology. Its use as a noninvasive tool will enable observation of morphologic changes that arise in the cone mosaic of TgP23H pigs over time.

**Translational Relevance:** Pigs are widely used for translational studies, and the ability to noninvasively assess cellular changes in the cone mosaic will facilitate more detailed investigations of new retinal disease models as well as outcomes of potential therapies.

## Introduction

Pigs (*Sus scrofa*) are a highly relevant research model and are widely used in translational research[1] due to their physiological and anatomical similarity to humans.[2] The pig is a particularly useful model for vision research because of its cone-rich central retina[3] and diurnal behavior. This area of increased cone density is known as the visual streak and is populated by both medium- and short-wavelength sensitive cone photoreceptors.[4] The visual streak in the pig is a useful analog of the human macula.[5] Because of the similarities to human anatomy, pigs have been used to test retinal prostheses,[6–8] allogenic[9,10] and xenogenic[11,12] retinal transplants, and in

gene therapy studies.[13–15] This widespread use as a preclinical model makes noninvasive ocular imaging increasingly important in order to observe disease progression[16] and therapeutic safety and efficacy in vivo.[17–19] While optical coherence tomography (OCT)[20,21] and scanning light ophthalmoscopy (SLO) are valuable tools that have been applied to study the gross anatomy of the pig retina, the use of pigs in gene and cell therapy creates a pressing need for cellular resolution, noninvasive imaging.

Adaptive optics SLO (AOSLO) corrects aberrations from the lens and cornea and enables cellular resolution imaging.[22] AOSLO is widely used in humans[23–30] and has been used in several other research models, including the tree shrew,[31] ground squirrel,[32] mouse,[33,34] rat,[35] cat,[36] chick,[37] and macaque.[38] Despite the advantages of the pig model, AOSLO imaging has not previously been used to study the pig retina. This represents a technological gap in our inability to evaluate disease progression, particularly of cone photoreceptors in pigs with retinal disease. Here, we demonstrate the use of AOSLO imaging of the photoreceptor mosaic (specifically the cone mosaic) in wild-type (WT) and transgenic rhodopsin P23H (TgP23H) pigs and correlate these images to OCT images and ex vivo microscopy.

## Methods

All animal research was conducted in accordance with the ARVO Statement for the Use of Animals in Ophthalmic and Vision Research, occurred in an AAALAC International approved research program, and was approved by the Institutional Animal Care and Use Committee at the Medical College of Wisconsin. The pigs were fed a swine-specific feed (Harlan Teklad Miniswine Diet 8753; Envigo, Hackensack, NJ) twice daily and provided water ad libitum through an automated water system. Additional fruit, vegetables, dog food, or ice cubes were provided as food enrichment. Rubber toys and blankets also were provided as enrichment. Pigs were kept on a 14/10-hour light/dark cycle.

### Imaging Preparation

We imaged 14 pigs in total. Three pigs were used to develop and test the imaging and histology methods. The remaining 11 were successfully imaged and included a postnatal day 240 (P240) pig, and five litter- and sex-matched pairs of WT and TgP23H pigs

at P3, P15, P30, P90, and P180 (eight females and three males; Oak Hill Genetics, Ewing, IL). The genotype of TgP23H and WT pigs were analyzed by PCR as previously described,[39] and TgP23H piglets were heterozygous.[39] For imaging, pigs were anesthetized and intubated for delivery of inhaled isoflurane (5% induction, 2%–3% maintenance, 1 L/min $O_2$). In pigs over 1 month old, an intramuscular dose of the muscle relaxant, tiletamine-zolazepam (Telazo, l7 mg/kg; Zoetis US, Parsippany, NY), was given prior to intubation. During anesthesia induction, the pupils were dilated and cycloplegia was induced with one drop each of 2.5% phenylephrine and 1% tropicamide. Peribulbar injections of 0.5 mL of a 1:1 mixture of 2% lidocaine:0.5% bupivacaine were administered using a 23-gauge needle into each quadrant of the eye to paralyze the extraocular muscles and provide procedural and postprocedural analgesia. Four scleral stay sutures (6.5-mm 3/8 circle spatula needle, 6-0 silk; Ethicon Inc., Somerville, NJ) were placed transconjunctively, oriented parallel to and just posterior to the limbus along the superior-inferior and nasal-temporal axes, to allow fine manipulation and stabilization of the eye and, in particular, for fine alignment of the fundus based on feedback from raw AOSLO videos.

We used a Barraquer lid speculum to retract the eyelid and administered saline drops as needed to maintain corneal lubrication. Body temperature was maintained (36°–39°C internal temperature) during the procedure using a warming pad (HotDog; Augustine Temperature Management, Eden Prairie, MN). Body temperature, heart rate, and respiratory rate were monitored throughout anesthesia, and intravenous fluids were given through an auricular venous catheter as needed. Following imaging, the stay sutures were removed and ophthalmic antibiotic ointment (Tobradex; Alcon, Fort Worth, TX) was applied. For terminal procedures, a pentobarbital-based solution (Beuthanasia-D Special, 0.22 mL/kg; Merck Animal Health, Madison, NJ) was injected intravenously, and the animal was monitored to ensure the irreversible cessation of respiratory and cardiac function.

### Imaging Setup

During AOSLO imaging, the pig's body was supported in a surgical V-trough and the head was supported on a custom head support to maximize steering and stability during imaging (Fig. 1). The head support was 3D-printed (ProJet 3500; 3DSystems, Rock Hill, SC) using acrylonitrile butadiene
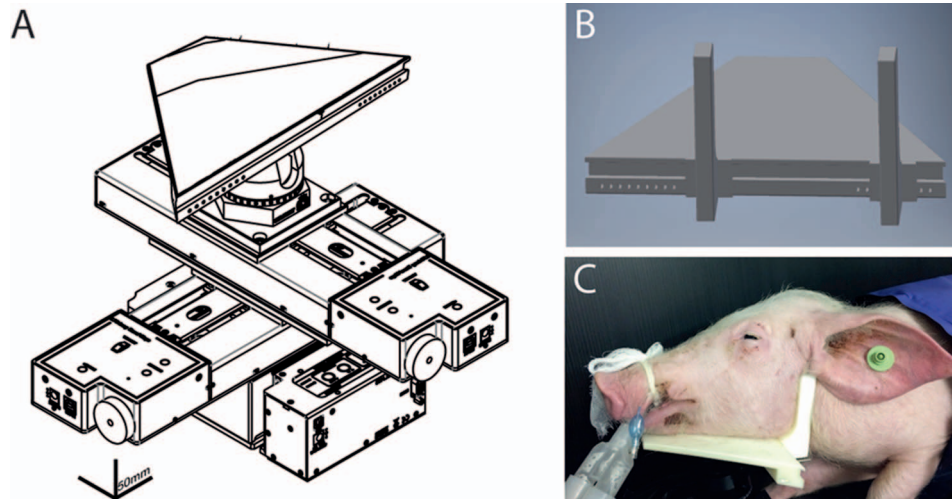
**Figure 1.** Apparatus for animal positioning for AOSLO imaging. Because the AOSLO is a fixed beam system, we took advantage of the cervical mobility of the pig and designed a custom 3D-printed plastic head mount, which was affixed to an articulating base, two motorized stages, and a motorized lab jack (CAD files from ThorLabs). This allowed rotation and translation of the pig's head in X, Y, and Z planes (A). The pig's body was supported separately. The head mount (B) rests under the chin, and the vertical supports rest against the neck. A system of pegs was used to adjust the position of the vertical supports. The head mount was designed so that the vertical supports fit snugly along the ramus of the mandible (C).

styrene–like plastic and included two vertical posts that could be adjusted and locked with aluminum dowels to secure the mandible in place (Fig. 1B, C). The head support was mounted on a translation/rotation system of two orthogonal, motorized translation stages (LTS150; ThorLabs, Newton, NJ), a motorized lab jack (MLJ150; ThorLabs), and an articulating base (SL20; ThorLabs) (Fig. 1A). The motorized components were controlled with software, (Kinesis; ThorLabs).

## Retinal Imaging: AOSLO

Pigs were imaged on a custom AOSLO system modified for a 4.5-mm pupil diameter.[40] We simultaneously collected confocal and nonconfocal videos with a minimum of 150 frames with 850 nm light for wavefront sensing, 790 nm light[41,42] for imaging AOSLO, videos were registered to a reference frame, and 20 to 100 frames were averaged as previously described.[43,44] AOSLO images were manually montaged using software (Photoshop CS6; Adobe Systems, Inc., San Jose, CA), and eccentricity of the AOSLO images were measured from the optic disk according to previously published topography.[4] AOSLO images were scaled by imaging vertical and horizontal lines with known spacing to obtain the degrees/pixel. This value was then adjusted by the ratio of the measured axial length to the reference axial length of 24 mm. This value was multiplied by

the retinal magnification factor previously derived from human optics of 291 μm/deg to obtain an estimate of the image scale in micrometers per pixel. We cropped 55 × 55-μm regions of interest from the split detector montage and counted the cones semiautomatically, using a previously described algorithm[45] and custom software (Translational Imaging Innovations, Inc., Hickory, NC). Split detector AOSLO images from P30 pigs were insufficient to resolve individual cones, and we instead counted cones using the confocal images in these animals. Images were counted by three observers (ALH, AES, and JC), who were masked to the pig genotype. We averaged cone counts across observers.

## Retinal Imaging: OCT

OCT images (12-mm nominal length, 1000 A-scans/B-scans, 48 repeated B-scans) were acquired using SD-OCT (Bioptigen Envisu R2200; Leica Microsystems, Inc., Buffalo Grove, IL) with a broadband source (central wavelength 878.4 nm, 186.3-nm bandwidth; Superlum; Enterprise Park, Cork, Ireland). Twenty B-scans were registered and averaged to a manually selected reference B-scan using the TurboReg plugin in ImageJ software (http://imagej.nih.gov/ij/; provided in the public domain by the National Institutes of Health, Bethesda, MD).[46,47] Scans were flattened to a semiautomatically generated retinal pigment epithelium (RPE) contour[48] using

custom software (MatLab; Mathworks, Natick, MA) and representative 50-pixel-wide longitudinal reflectivity profiles were generated in ImageJ.[49,50] Axial length was measured using an ultrasound A-scan (OTI-Scan 1000; OTI Ophthalmic Technologies, Inc., Toronto, ON, Canada). The OCT lateral scale was calculated by multiplying the nominal scan length by the ratio of the axial length to the Bioptigen's assumed axial length of 24 mm.

## Retinal Imaging: Funduscopy

An average of 100 wide-angle 55° fundus photos were acquired at 820 nm in the ART mode on a custom multiline cSLO (modified Spectralis HRA, version 1.9.1.3.0; Heidelberg Engineering, Heidelberg, Germany). At the same time, a wide-angle fundus image also was acquired (RetCam; Clarity Medical Systems USA, Pleasanton, CA). Different imaging modalities were scaled, overlaid, and aligned in Photoshop, using retinal vasculature as the reference. Retinal blood vessels were manually traced from the montaged cSLO, OCT, and RetCam images in Photoshop to generate schematic figures for demonstrating the approximate location of the retinal images shown in Figures 3 to 7.

## Histology

Eyes from all animals were removed immediately following cessation of heartbeats, and circumferential cuts were made in the globe at the ora serrata to remove the anterior segment. Eyecups were fixed in 4% paraformaldehyde for 24 hours immediately following enucleation and dissection. After fixation, the retina was dissected from the RPE and radial cuts made toward the optic nerve. The retina was then flat-mounted with the outer retina facing up. The samples were imaged for differential interference contrast (DIC) histology on a microscope (LSM 510; Carl Zeiss, Jena, Germany) with a 633-nm laser at 10% power. Cones from histology images were manually counted by a single observer (ALH), and Voronoi diagrams were generated using custom software (Translation Imaging Innovations, Inc.). The Voronoi domain of a given cone is defined as all pixels in the image plane that are closer to that cone than to any other. From this, the area and number of sides of each Voronoi domain are calculated.[51] Voronoi regularity was determined by dividing the mean Voronoi area of all bounded cones by the standard deviation of the Voronoi areas of all bounded cones in that image.

# Results

## Comparisons of Human and Pig Retinal Images

OCT B-scans illustrate several differences between humans and pigs (Figs. 2A, C and B, D, respectively). In humans, the thickest point of the retina is perifoveal, and the highest cone density occurs in the fovea. In pigs, the thickest point of the retina, the area centralis, also contains the highest cone density. The high-resolution OCT B-scans from the human perifovea (Fig. 2C) and the pig area centralis (Fig. 2D) illustrate the differences in the retinal band structure of humans and pigs. The human OCT (Fig. 2C) shows four hyperreflective outer retinal bands that correspond to the external limiting membrane (ELM), the ellipsoid zone (EZ), the interdigitation zone (IZ), and the RPE.[52] The pig OCT (Fig. 2D) shows five hyperreflective outer retinal bands that correspond to the ELM, which appears fainter than in humans, and two sets of doublet bands, which correspond to the photoreceptors (EZ) and the RPE (Fig. 2B). AOSLO retinal images illustrate the similarities between the human (Fig. 2E, G) and pig (Fig. 2F, H) retina. In the confocal images from both pigs and humans (Fig. 2E, F), the cones appear as bright, punctate spots, and in the AOSLO split detector images (Fig. 2G, H), cone inner segments appear as distinct bumps.

We compared cone density estimates from AOSLO images to those from histology in this WT pig retina at several retinal locations and found AOSLO slightly underestimated cones (Fig. 3). Specifically, comparisons of two different isoeccentric regions in this P240 WT pig show $14,000 \pm 500$ cones/mm$^2$ on AOSLO (Fig. 3B$_1$, B$_2$) versus 16,000 cones/mm$^2$ on DIC (Fig. 3C) and $6500 \pm 500$ cones/mm$^2$ on AOSLO (Fig. 3D$_1$, D$_2$) versus 7000 cones/mm$^2$ on DIC (Fig. 3E), a range of 12.5% to 7.1%, respectively.

## Retinal Structure of WT and TgP23H Pigs Assessed with OCT

We examined the superior retina of TgP23H pigs using AOSLO, OCT, and histology and identified distinct changes in their photoreceptors across ages. Schematic diagrams of each are shown for P30, P90, P180 (Figs. 4A, F, and J, respectively), along with P180 WT littermate control (Fig. 4O). P3 and P15 TgP23H and WT littermates were examined with OCT only (see Fig. 5). As noted above, all WT pigs, regardless of age (P 30, 90, and 180), had five
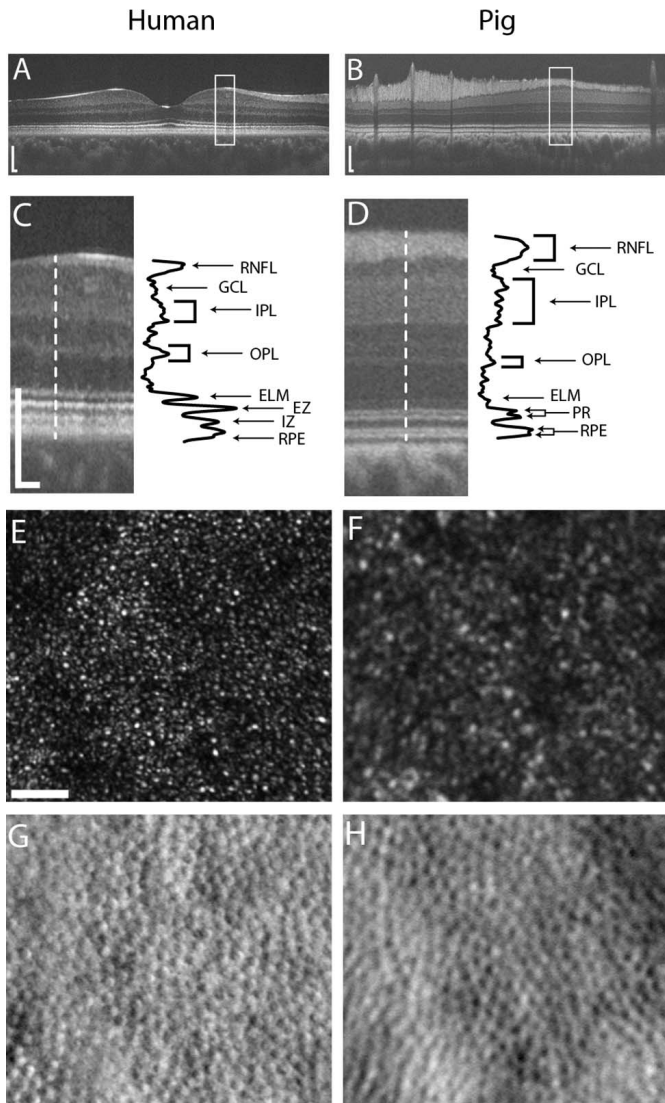
## Human



## Pig

**Figure 2.** Comparison of human and porcine retinal images. OCT line scans of human (A) and pig (B) retinas show morphologic differences. Magnifications of OCT B-scan images show marked differences in the thickness of the various retinal layers between the human (C) and the pig (D). Four hyperreflective outer retinal bands are typically resolved in humans (ELM, EZ, IZ, RPE) (C), whereas pigs show a different appearance, with two closely spaced "doublet" bands (PR, RPE) (D). Confocal AOSLO images of the photoreceptor mosaic acquired at 4° superior to the fovea in a 22-year-old human (E) and near the superior edge of the central streak in a P180 WT pig (F) show that the cones and their mosaic are similar in appearance. The cones have a Gaussian-like reflectivity profile on confocal imaging due to wave guiding within the cone. Split detector images at the same locations also appear similar between species (G, H), with the circular structures in these images likely originating from cone inner segments. Human images were collected under an institutional review board–approved protocol in accordance with the Declaration of Helsinki. The human OCT was acquired on a Bioptigen OCT, and the AOSLO images were acquired on a system identical to that described in the Methods section here, but without the pupil modifications. *Scale bar*: 200 μm in OCT; 25 μm in AOSLO.

hyperreflective outer retinal bands (Fig. 2C, Fig. 4P, Fig. 5). In contrast, the innermost doublet (corresponding to the photoreceptors) was disrupted in TgP23H pigs, although the outermost doublet that represents the RPE remained intact. This altered outer retinal reflectivity was evident in the youngest animals (P3, Figs. 5A and B, Tg and WT, respectively), and the extent of disruption worsened with age (Fig. 5). Consistent with our published observations that only a single layer of cones remains,[53] the OCT B-scan from a P180 TgP23H pig showed a similar outer retinal band structure between the optic nerve and midperipheral retina (left and right, respectively; Fig. 6A).

The TgP23H pig retina also shows a hyperreflective signal positioned within the inner nuclear layer (INL) and was seen at all ages examined (Figs. 4B, G, K). This band also is often seen in WT retina, although its contrast within the INL is variable (Fig. 5). Preliminary experiments suggest that this band corresponds to a vascular plexus in the INL (data not shown).

## AOSLO Estimates of Cone Density

The higher lateral resolution provided by AOSLO offers a more detailed view of cone degeneration in the TgP23H retina. In the WT pig at P180, AOSLO images (Fig. 4Q, R) show a robust homogenous cone mosaic, and a consistent confocal AOSLO signal also is observed. At P30, cone density estimates from isoeccentric images from WT and TgP23H littermates within the visual streak (Fig. 4C) show no appreciable difference (23,100 ± 4900 vs. 20,800 ± 4900 cones/mm$^2$, WT versus TgP23H, respectively). Even at P90 (Fig. 4I; 14,000 ± 1800 vs. 15,000 ± 1800 cones/mm$^2$, respectively) and P180 (Fig. 4R; 14,800 ± 1000 versus Fig. 4M; 16,300 ± 6700, there is only a small difference in cone density between WT and TgP23H retinas. Images of the cones identified in each ROI are shown in Supplementary Figure S1. As can be seen, cones identified in the split detector AOSLO images of P90 and 180 TgP23H pigs (Fig. 4I, M) were qualitatively more variable in their appearance compared to WT (Fig. 4R). Some TgP23H cones maintained a clear shadowing pattern, others showed a less pronounced pattern.

## AOSLO Underestimates Cone Density Compared to Histologic Estimates

As described above for P240 WT retina, cone density measured from isoeccentric DIC microscopic images (histology) typically slightly overestimates
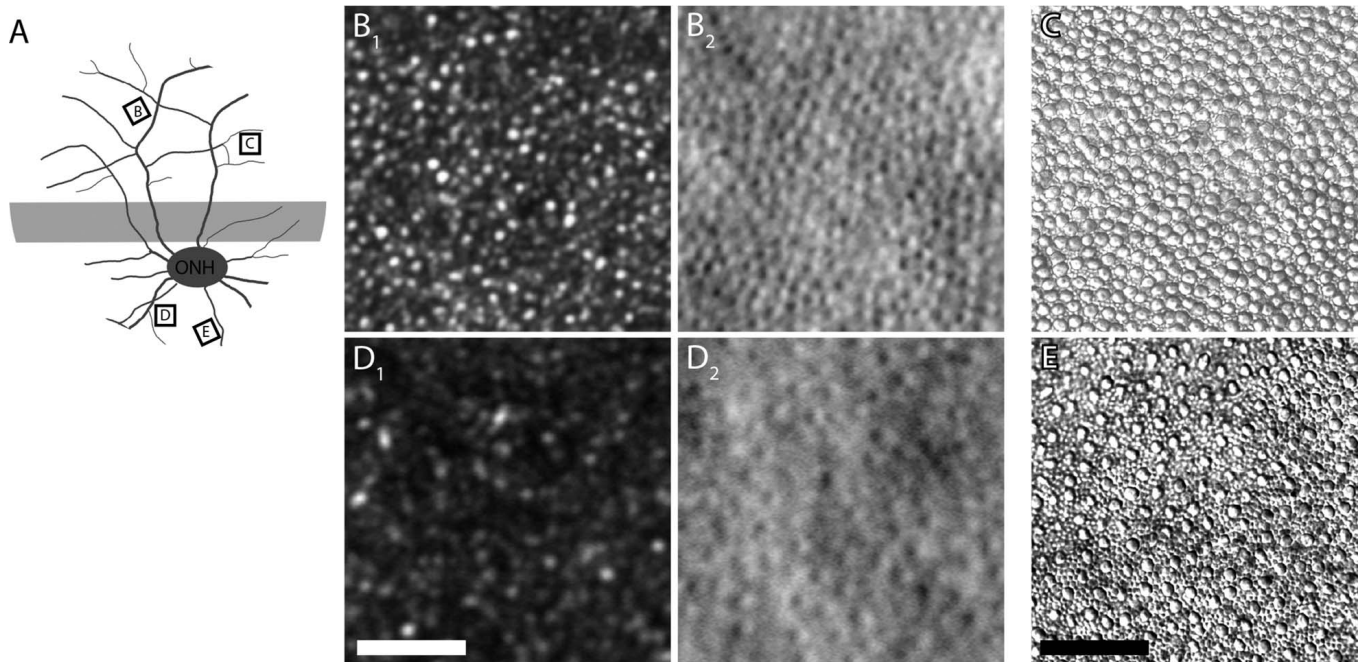
**Figure 3.** Correlative histology of the pig cone mosaic. A schematic of the retinal fundus (A) shows the location of the visual streak (*gray*), as well as the locations of the AOSLO imaging ($B_1$, $D_1$ confocal; $B_2$, $D_2$ split detector) and histology (C, E) in an P240 WT pig. Estimates of cone density above the central streak from histology (C) are 16.9% higher compared to AOSLO (B). Similarly, AOSLO estimates of cone density in regions from below the optic nerve (D, E) are lower (10.0%) than histology. *Scale bars*: 50 μm.

cone density evaluated from AOSLO images. Cone density also was underestimated in the WT pig at P180 (Fig. 4S) with an estimate of 14,800 cones/mm$^2$ on AOSLO and 18,700 cones/mm$^2$ on histology (a 20.9% difference). Similarly, estimates from AOSLO were slightly lower than histology for the P30 TgP23H pig (Fig. 4E; 20,800 cones/mm$^2$ versus 23,600 cones/mm$^2$, an 11.9% difference). In contrast, we estimated cone density from AOSLO images (Fig. 4N) of the P180 TgP23H pig and found 16,300 cones/mm$^2$, whereas we estimated only 9900 cones/mm$^2$ on histology (a 64.6% difference). This difference likely results from the range of appearances of degenerating cones in the TgP23H retina and different criteria across observers for what is considered a cone. The cone estimates across our three observers were quite variable in the P180 TgP23H pig, ranging from 8900 to 22,000 cones/mm$^2$. Despite this, the overall tendency is that AOSLO-based estimates of cone density are lower than those from histology.

We found a progressive decline in cone density in the P90 TgP23H pig with increasing distance from the optic nerve head (ONH) (3.5, 5.5, and 7 mm superior to the ONH and $31,600 \pm 6100$; $23,300 \pm 10,500$; and $13,700 \pm 1300$ cones/mm$^2$, respectively [Fig. 6B–D]). Cone densities in this P90 TgP23H pig at 3.5 and 5.5

mm are similar to previously published cone densities in the WT pig.[4] In contrast, cone density at 7 mm above the optic nerve is lower than that reported in previously published topographical reports, although the topographical data does not include error for their estimates.[4] AOSLO split detector images of the cone inner segments show variability in the TgP23H pig at 7 mm, 5.5 mm above the optic nerve, and also show variability in their appearance on split detector, with some cones appearing more well-formed and distinct (Fig. 6C, D).

Cone degeneration alters the regularity of the cone mosaic.[51,54] Histology from the P180 WT pig shows a regular photoreceptor mosaic, with a Voronoi area regularity index of 7.96 (Fig. 7B–D). This is similar to the Voronoi area regularity seen in the normal human retina.[51] Isoeccentric histology from the P180 TgP23H littermate shows focal cone loss and a smaller Voronoi area regularity index, 4.04 (Fig. 7F–H) and 4.61 (Fig. 7J–L). In this animal, at 3.5 mm above the optic nerve (Fig. 7N–P), we found a regular and preserved cone mosaic whose Voronoi area regularity index was 7.78. These data corroborate the progressive decrease in cone density observed in vivo (Fig. 6) and provide evidence that regularity is useful as a biomarker for disease progression.

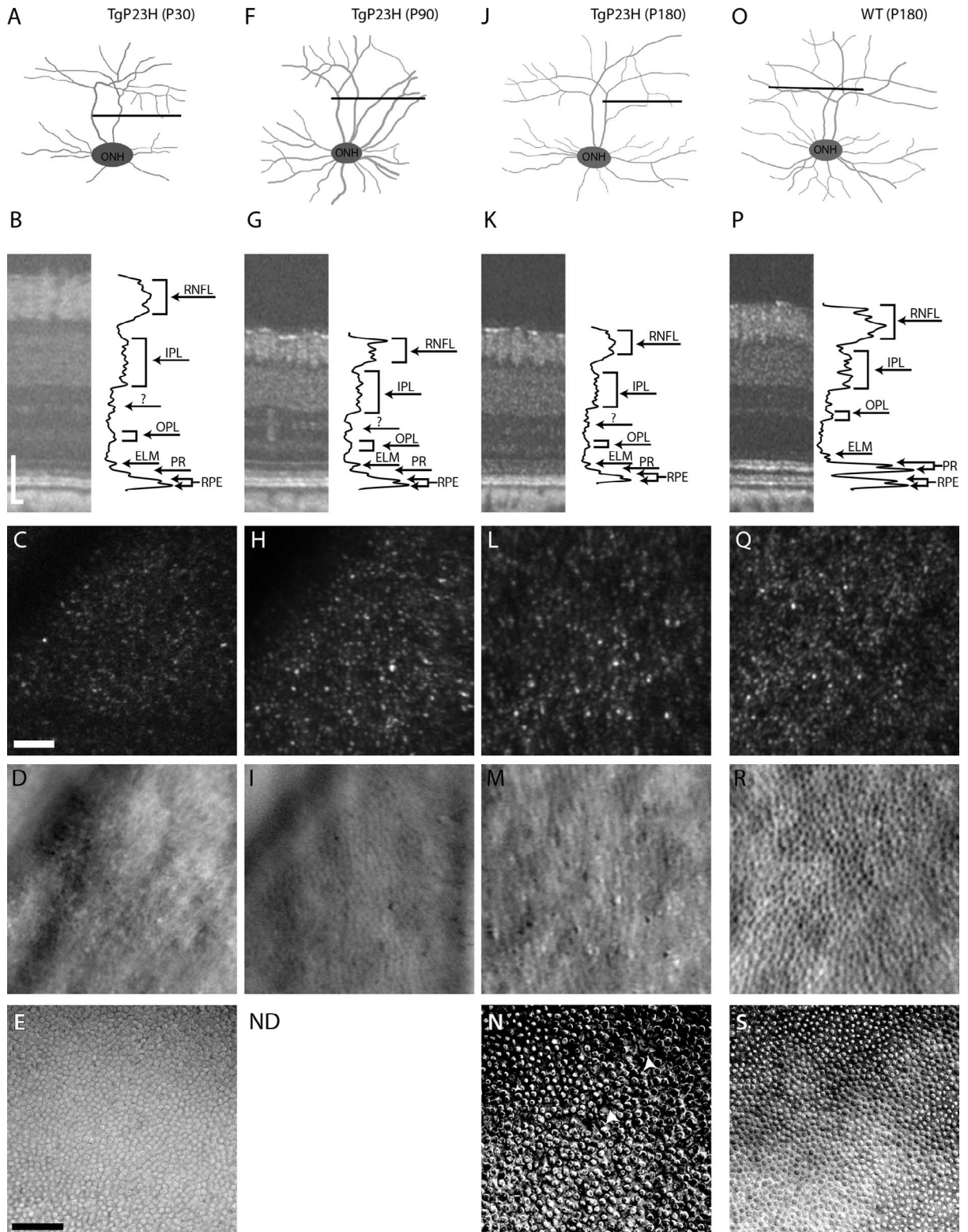**Figure 4.** Cross-sectional imaging of the TgP23H pig retina at different ages and stages of photoreceptor degeneration. A schematic of the retina shows the position of the OCT and the approximate location of the AOSLO and DIC histology for the P30 TgP23H pig (A–E), the P90 TgP23H pig (F–I), the P180 TgP23H pig (J–N), and the P180 WT pig (also shown in Fig. 2) (O–S). OCT B-scans from the TgP23H pigs (B, G, K), show that the signal from the photoreceptor doublet bands is attenuated and that the ONL thickness decreases. By comparison,
→

←

the OCT B-scan of the P180 WT pig (P) shows conserved outer retinal bands with two doublets. A diminished, more punctate confocal AOSLO signal is observed in TgP23H pigs (C, H, L) compared to the robust confocal signal in the P180 WT pig (Q). The TgP23H pigs have a heterogenous appearance on the split detector AOSLO (D, I, M) with variable cone appearance, while the split detector in the WT pig (R) shows a homogenous cone mosaic with the distinct bumps. Histology of the P30 pig (E) shows a contiguous cone mosaic with cones abutting and no gaps between cones since most of the rods have been lost.[66] At 6 months of age, histology from the P180 TgP23H pig (N) shows a noncontiguous cone mosaic with multiple gaps (*arrowheads*). Histology at an isoeccentric location in a P180 WT littermate (S) shows regularly shaped circular cones, with gaps between the cones where the rods are located. *Scale bars*: 50 μm, AOSLO and histology; 100 μm OCT. ND, no data available.

## Discussion

Here we applied the noninvasive imaging techniques, AOSLO and OCT, to examine a porcine model of retinitis pigmentosa. Our results demonstrate their potential for sequential assessment of normal and TgP23H pig retinal structure in vivo. OCT images of the pig retina have been previously published by several groups,[20,21,55,56] and our obser-
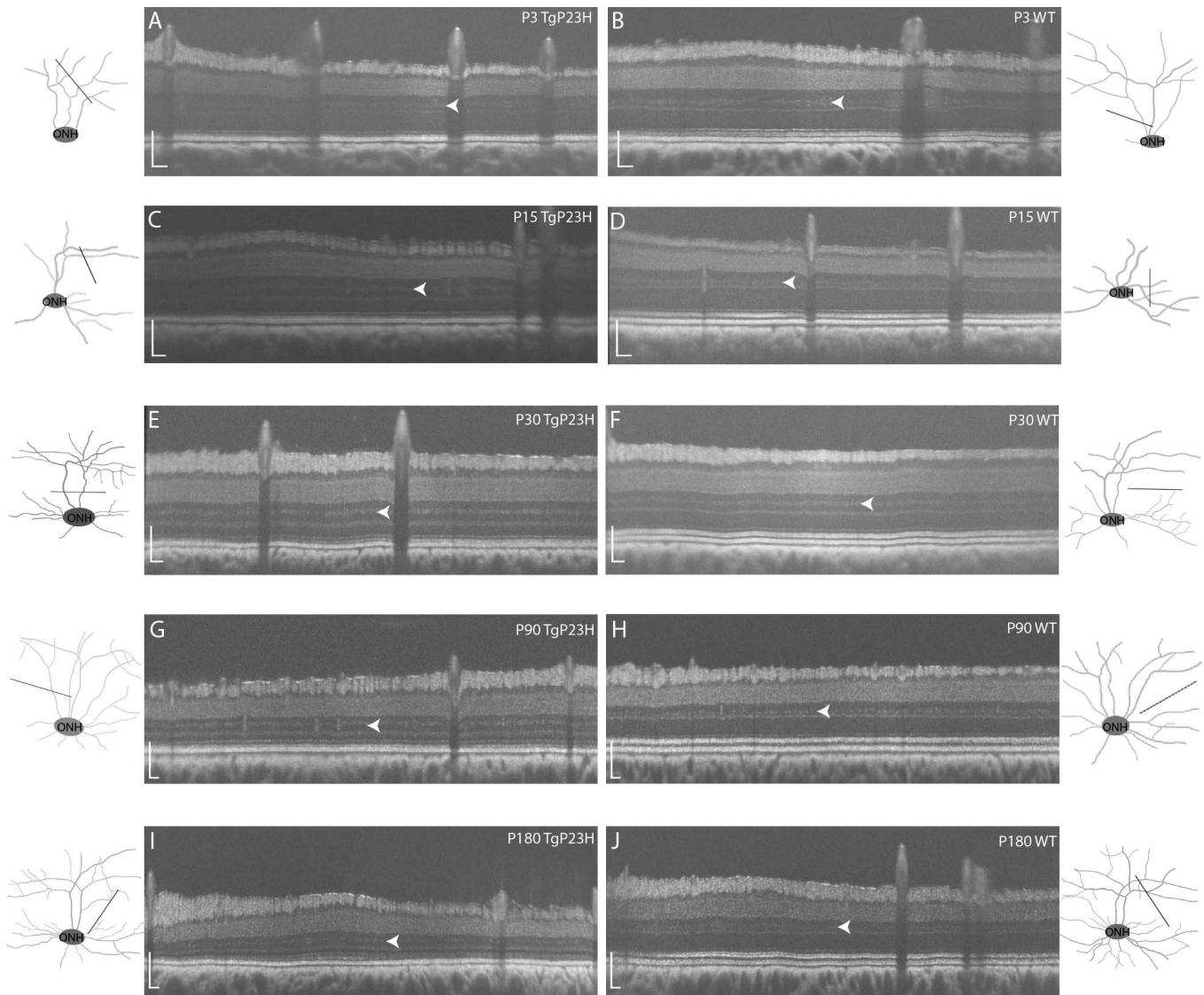


**Figure 5.** OCT overviews from transgenic and WT littermates. OCT images show loss of one of the bands within the photoreceptor doublet in TgP23H pigs at all ages (A, C, E, G, I), while WT pigs show the typical five outer retinal bands (B, D, F, H, J). An additional hyperreflective band in the INL is indicated with *white arrowheads*. (E, I, J) Separate OCT scans from the same eye shown in Figure 4, and (G) is the contralateral eye of the same animal shown in Figure 4. *Vertical* and *horizontal scale bars*: 200 μm.
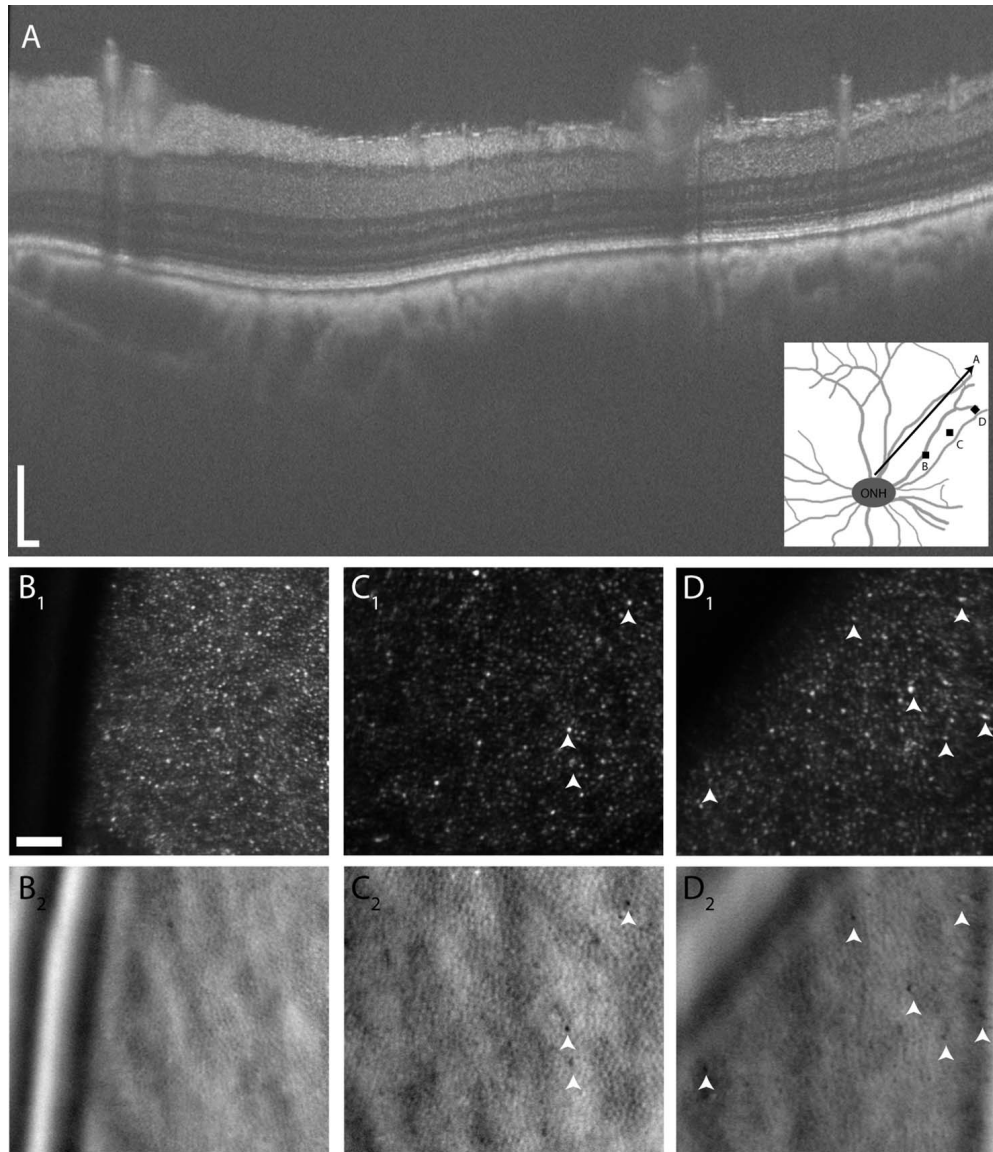
**Figure 6.** AOSLO detects heterogeneity in P90 TgP23H pig retina (same animal as Fig. 4F–I). A schematic of the fundus (*inset*) shows the location of an OCT B-Scan (A) and AOSLO images from locations 3.5 mm ($B_{1,2}$), 5.5 mm ($C_{1,2}$), and 7 mm ($D_{1,2}$) superior to the ONH. In the B-scan, the banding pattern appears homogeneous from near the ONH (*left*) to ~9 mm distal to the ONH. In contrast, the AOSLO images detect differences at these locations. At 3.5 mm from the ONH, the cone mosaic appears homogenous, with no irregular cone inner segments observed on split detector images ($B_2$), and multiple bright spots are observed on confocal images ($B_1$). In the midperiphery (C), several distinct cones (*white arrowheads*) are still seen on the split detector images ($C_2$), and these distinct cones seem to correlate with brighter confocal signal ($C_1$). At 7 mm from the ONH (D), there is a heterogenous appearance of cones on split detector ($D_2$), and several cones having altered shadowing (*white arrowheads*) seem to correlate with a bright confocal signal ($D_1$). *Scale bars*: 200 μm on OCT image both vertically and horizontally; 50 μm on AOSLO images.

vations and interpretation of the outer retinal hyper-reflective bands differ. These previous studies typically identify three hyperreflective outer retinal bands, whereas our images clearly show that five bands exist in the WT pig. The innermost (anterior) hyperreflective band in our images seems certain to originate from the ELM, whereas the two sets of "doublet" hyper-reflective bands likely arise from the photoreceptor and RPE layers, respectively. This hypothesis is reinforced as the innermost doublet band is significantly altered in the TgP23H retina. The discrepancy across the datasets likely results from differences in imaging methodology across laboratories. In contrast to our approach, one study removed the anterior
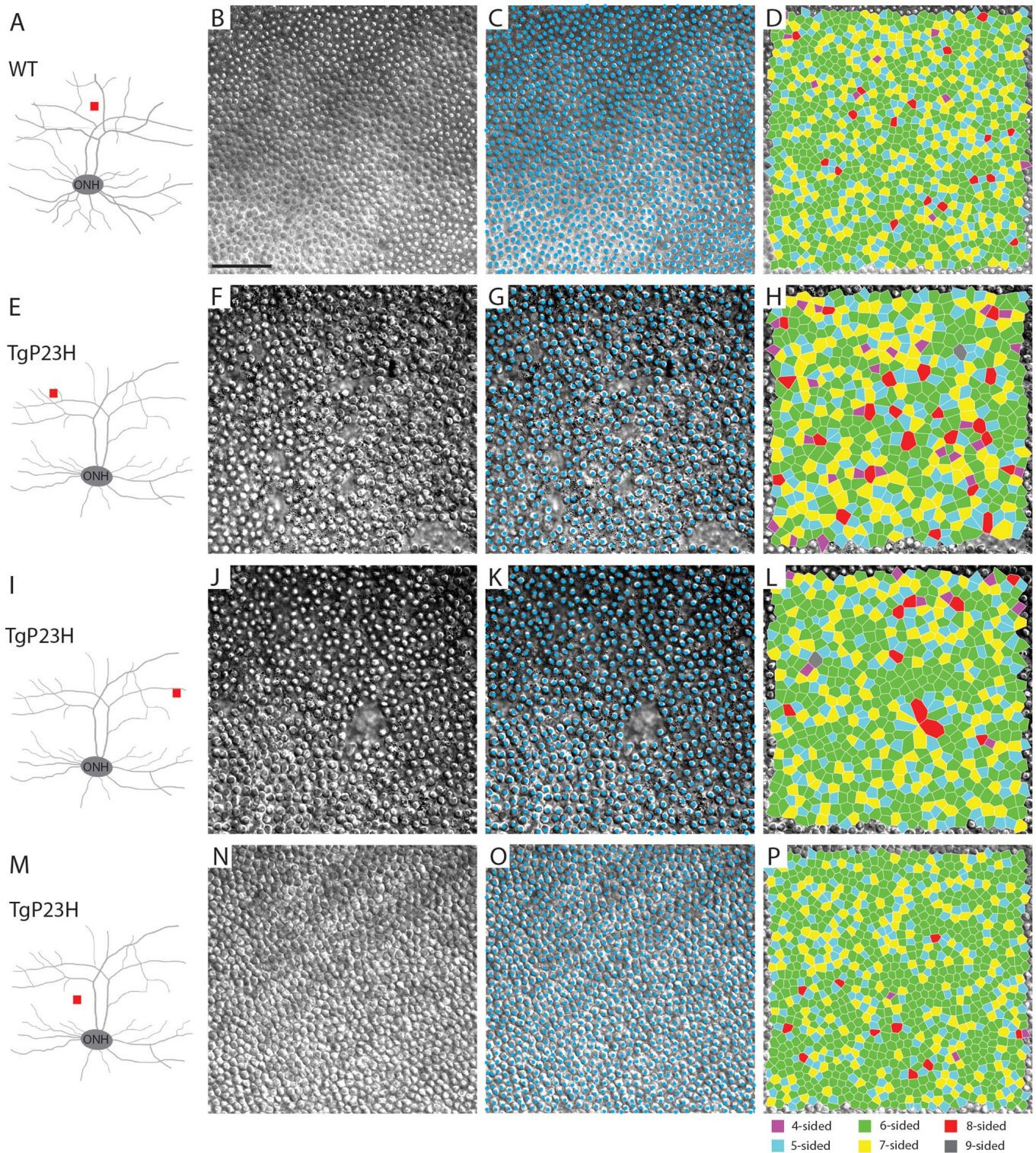
| | | |
|---|---|---|
| ■ 4-sided (magenta) | ■ 6-sided (green) | ■ 8-sided (red) |
| ■ 5-sided (cyan) | ■ 7-sided (yellow) | ■ 9-sided (gray) |

**Figure 7.** Quantitative analyses show decreased cone mosaic regularity in P180 TgP23H pig. DIC images of the P180 WT pig (same animal as in Fig. 4O–S) (A) show a regular mosaic (B–D) and a Voronoi index similar to that seen in the normal human retina (see text). The same analyses of isoeccentric regions (E, I) from a TgP23H littermate (same pig as in Fig. 4J–N) show increased irregularity (F–H, J–L) of the cone mosaic (see text). Histology from a location closer to the ONH (M) in this TgP23H littermate shows a more regular cone mosaic (N–P), similar to WT. On Voronoi color overlays, *gray* = nine-sided, *red* = eight-sided, *yellow* = seven-sided, *green* = six-sided, *cyan* = five-sided, and *magenta* = four-sided. *Scale bar*: 50 μm.

segment of the eye prior to OCT imaging.[20] The image resolution in a second study was insufficient to distinguish either sets of doublets,[21] and it is noted that some of their OCTs occurred ex vivo. Indeed, when we attempted to image the retina both pre- and immediately post euthanasia, resolution declined as we also could not resolve the doublets (data not shown). This indicates that even brief anoxia causes changes to the delicate photoreceptor outer segments and alters their appearance on OCT.

Another impediment to obtaining high-resolution images is corneal drying. Corneal surface drying alters optical quality and creates anterior segment opacities. Uneven or inadequate tear film will decrease the signal and resolution of retinal bands by introducing large aberrations[57] and may explain why the hyper-reflective bands reported in other publications appear darker than our images.[50,58] We find that not all lubrication is equally effective. We use saline drops to maintain corneal lubrication (Piri N, et al. *IOVS.* 2018;59:ARVO E-abstract 729)[56] and find that the application of Gonak deteriorates the resolution of the OCT images (data not shown).

The hyperreflective band in the INL, to our knowledge, also has not been previously reported[20,21] and is more evident in young WT pigs and in TgP23H retinas regardless of age (Fig. 5). The location of this band in the TgP23H retinas appears to change with rod photoreceptor degeneration. We conjecture that this band is located in the INL and appears to move as the outer nuclear layer (ONL) shrinks. A more systematic investigation is underway to determine the origin of this band and why it is more prominent in some animals.

In the OCT images from the TgP23H animals, the innermost doublet, ascribed to the photoreceptors in WT retina, appears as a single hyperreflective band up to P90 (Fig. 4). Given the previous studies of rods in these TgP23H pigs, this change must be correlated with rod cell death. The single retained hyperreflective photoreceptor band likely represents the retained cone structure observed with both AOSLO and on histology. Indeed, the ultrastructure of TgP23H pig cone photoreceptor outer segments is similar to WT at P3.[59]

The outer retinal OCT hyperreflective band appears consistent at retinal locations across the OCT scan (Fig. 6A), which is somewhat inconsistent with cone loss at the same locations using AOSLO imaging (Fig. 6B–D). Similarly, the OCT outer retinal hyperreflective band in the TgP23H pigs was similar at P30, P90, and P180, despite progressive changes on AOSLO (Fig. 4). This suggests that the OCT hyper-reflective outer retinal band representing cones does not accurately reflect changes in cone density and/or subcellular changes in cone morphology. This indicates that AOSLO would be the preferred approach when evaluating cellular-based therapies aimed at restoring cone outer segment structure. Despite the limitation in the OCT, it accurately reflects changes in ONL thickness as a function of age in the TgP23H pig, indicating that it is a useful biomarker for monitoring disease progression and any therapy that arrests rod degeneration.

Previous studies have characterized retinal morphology and function in the TgP23H pig model using histology and ERG (Piri N., et al., *IOVS.* 2018;59: ARVO E-abstract 729)[39,53,60] and shown that cone inner segments are maintained until ∼1 year of age, although they appear dysmorphic, for example, swollen.[39] This change is reflected in our AOSLO images, which show residual inner segments at P180, and our split detector images, which show a heterogeneity among TgP23H cone inner segments, with some showing exaggerated shadowing. AOSLO imaging estimates that cone densities in the P90 TgP23H pig are similar to published estimates of WT pig histology at 3.5 and 5.5 mm and are slightly lower at 7.5 mm. Previous studies have focused on the time course of rod degeneration,[53,59] and our current studies complement these by examining the pattern of cone degeneration. Our data suggest that decreased cone density is first observed in the superior retina, although this relationship needs to be more thoroughly explored. It also remains to be determined what the relationship is between the irregular cones observed in earlier disease stages and the swollen, surviving cone inner segments observed on histology. As mentioned above, corneal hydration is crucial to high OCT resolution, and this was even more problematic with AOSLO imaging. This limitation precluded longitudinal AOSLO imaging of individual pigs, but with these impediments defined, we are confident we can develop an approach so that AOSLO can be used for sequential imaging.

Our estimates of cone densities from AOSLO and DIC histology are generally similar to previously published results.[3,4] Our DIC imaging shows reasonable agreement with our cone estimates from the AOSLO split detector images, although AOSLO consistently underestimated DIC by 13.1% on average. One source of the difference between AOSLO and histology estimates can be attributed to tissue shrinkage during histologic processing, which would increase the density; we did not estimate shrinkage.[61] Differ-

ences also could arise from errors in the optical scaling model used to estimate the scale of our AOSLO retinal images. In fact, it will be necessary to adjust the scaling when imaging the same animal over time as the eye grows larger (a change from neonate [~19 mm] to adult pig [~24 mm], ~5 mm in diameter).

Our AOSLO cone estimates were variable across observers; the standard deviation between cone count estimates from our three observers ranged from 500 to 10,500 cones/mm$^2$. Repeatability was calculated to be 12,900 cones/mm$^2$, meaning that the difference between two measurements would be expected to be less than this value for 95% of pairs of measurements. This substantial range also has been noted in AOSLO images of the human retina,[62–65] where low signal images lead to wide variability in an observer's cone estimates.[63] Consistent with this idea, counts across observers were most consistent in the P240 WT pig (Fig. 3), which had the best signal and the most consistent cone morphology on the AOSLO images. An additional factor could be slight variation in the location between the AOSLO imaging and the histology. Although we made every effort to sample from similar retinal regions, the precise location and/ or overlap of the images was not perfect. Finally, the stage of photoreceptor degeneration also may influence the quality of the signal.

In our larger animals, we experience another limitation to AOSLO imaging with our current system where the imaging beams are stationary. Small animals[31–33] are easier to move to accommodate the stationary beams, but a 40- or 80-kg pig is more problematic. Even so, we were able to sample a relatively wide range of retinal locations by leveraging the relative flexibility of the pig's cervical spine to position the head and using stay sutures to position the eye. These limitations also will have to be addressed, and we anticipate that they will be as interest grows in the pig as a model. These technical challenges also added to our difficulty in performing longitudinal AOSLO imaging of a single animal.

While work remains, our results clearly demonstrate the utility of the AOSLO approach to evaluate cone photoreceptors in the living pig retina and its potential to evaluate cellular-level changes when studying retinal disease and assessing therapeutic outcomes.

## Acknowledgments

## References

1. Stricker-Krongrad A, Shoemake CR, Bouchard GF. The miniature swine as a model in experimental and translational medicine. *Toxicol Pathol.* 2016;44:612–623.
2. Swindle MM, Makin A, Herron AJ, Clubb FJ Jr, Frazier KS. Swine as models in biomedical research and toxicology testing. *Vet Pathol.* 2012;49:344–356.
3. Chandler MJ, Smith PJ, Samuelson DA, MacKay EO. Photoreceptor density of the domestic pig retina. *Vet Ophthalmol.* 1999;2:179–184.

4. Hendrickson A, Hicks D. Distribution and density of medium- and short-wavelength selective cones in the domestic pig retina. *Exp Eye Res*. 2002;74:435–444.

5. Kostic C, Arsenijevic Y. Animal modelling for inherited central vision loss. *J Pathol*. 2016;238:300–310.

6. Sachs HG, Gekeler F, Schwahn H, et al. Implantation of stimulation electrodes in the subretinal space to demonstrate cortical responses in Yucatan minipig in the course of visual prosthesis development. *Eur J Ophthalmol*. 2005;15:493–499.

7. Gekeler F, Szurman P, Grisanti S, et al. Compound subretinal prostheses with extraocular parts designed for human trials: successful long-term implantation in pigs. *Graefes Arch Clin Exp Ophthalmol*. 2007;245:230–241.

8. Adekunle AN, Adkins A, Wang W, et al. Integration of perforated subretinal prostheses with retinal tissue. *Transl Vis Sci Technol*. 2015;4:5.

9. Ghosh F, Wong F, Johansson K, Bruun A, Petters RM. Transplantation of full-thickness retina in the rhodopsin transgenic pig. *Retina*. 2004;24:98–109.

10. Klassen H, Kiilgaard JF, Zahir T, et al. Progenitor cells from the porcine neural retina express photoreceptor markers after transplantation to the subretinal space of allorecipients. *Stem Cells*. 2007;25:1222–1230.

11. Li SY, Yin ZQ, Chen SJ, Chen LF, Liu Y. Rescue from light-induced retinal degeneration by human fetal retinal transplantation in minipigs. *Curr Eye Res*. 2009;34:523–535.

12. Warfvinge K, Kiilgaard JF, Klassen H, et al. Retinal progenitor cell xenografts to the pig retina: immunological reactions. *Cell Transplant*. 2006;15:603–612.

13. Puppo A, Bello A, Manfredi A, et al. Recombinant vectors based on porcine adeno-associated viral serotypes transduce the murine and pig retina. *PLoS One*. 2013;8:e59025.

14. Colella P, Trapani I, Cesi G, et al. Efficient gene delivery to the cone-enriched pig retina by dual AAV vectors. *Gene Ther*. 2014;21:450–456.

15. Mussolino C, della Corte M, Rossi S, et al. AAV-mediated photoreceptor transduction of the pig cone-enriched retina. *Gene Ther*. 2011;18:637–645.

16. Hoerauf H, Brix A, Winkler J, et al. Photoablation of inner limiting membrane and inner retinal layers using the erbium:YAG-laser: an in vitro study. *Lasers Surg Med*. 2006;38:52–61.

17. Koss MJ, Falabella P, Stefanini FR, et al. Subretinal implantation of a monolayer of human embryonic stem cell-derived retinal pigment epithelium: a feasibility and safety study in Yucatán minipigs. *Graefes Arch Clin Exp Ophthalmol*. 2016;254:1553–1565.

18. Sørensen NF, Ejstrup R, Svahn TF, Sander B, Kiilgaard J, la Cour M. The effect of subretinal viscoelastics on the porcine retinal function. *Graefes Arch Clin Exp Ophthalmol*. 2012;250:79–86.

19. Barakat MR, Shusterman M, Moshfeghi D, Danis R, Gertner M, Singh RP. Pilot study of the delivery of microcollimated pars plana external beam radiation in porcine eyes. *JAMA Ophthalmol*. 2011;129:628–632.

20. Gloesmann M, Hermann B, Schubert C, Sattmann H, Ahnelt PK, Drexler W. Histologic correlation of pig retina radial stratification with ultrahigh-resolution optical coherence tomography. *Invest Ophthalmol Vis Sci*. 2003;44:1696–1703.

21. Cheng J, Sohn EH, Jiao C, et al. Correlation of optical coherence tomography and retinal histology in normal and Pro23His retinal degeneration pig. *Transl Vis Sci Technol*. 2018;7.

22. Roorda A, Romero-Borja F, Donnelly WJ 3rd, Queener H, Hebert T, Campbell M. Adaptive optics scanning laser ophthalmoscopy. *Opt Express*. 2002;10:405–412.

23. Duncan JL, Zhang Y, Gandhi J, et al. High-resolution imaging with adaptive optics in patients with inherited retinal degeneration. *Invest Ophthalmol Vis Sci*. 2007;48:3283–3291.

24. Carroll J, Neitz M, Hofer H, Neitz J, Williams DR. Functional photoreceptor loss revealed with adaptive optics: an alternate cause of color blindness. *Proc Natl Acad Sci U S A*. 2004;101:8461–8466.

25. Carroll J, Banin E, Hunt DM, et al. Evaluating the photoreceptor mosaic in blue cone monochromacy (BCM). *Invest Ophthalmol Vis Sci*. 2010;51:2935.

26. Langlo C, Denney D, Cooper R, et al. High-resolution imaging of retinal structure in retinitis pigmentosa and Usher syndrome. *Invest Ophthalmol Vis Sci*. 2013;54:655.

27. Chen Y, Ratnam K, Sundquist SM, et al. Cone photoreceptor abnormalities correlate with vision loss in patients with Stargardt disease. *Invest Ophthalmol Vis Sci*. 2011;52:3281–3292.

28. Morgan JIW, Chung DC, Nozato K, Maguire AM, Bennett J. Imaging retinal structure in

patients and carriers of choroidermia. *Invest Ophthalmol Vis Sci*. 2012;53:4648.

29. Rossi EA, Rangel-Fonseca P, Parkins K, et al. In vivo imaging of retinal pigment epithelium cells in age related macular degeneration. *Biomed Opt Express*. 2013;4:2527–2539.

30. Langlo CS, Patterson EJ, Higgins BP, et al. Residual foveal cone structure in *CNGB3*-associated achromatopsia. *Invest Ophthalmol Vis Sci*. 2016;57:3984–3995.

31. Sajdak BS, Salmon AE, Cava JA, et al. Noninvasive imaging of the tree shrew eye: wavefront analysis and retinal imaging with correlative histology. *Exp Eye Res*. 2019;185:107683.

32. Sajdak B, Sulai YN, Langlo CS, et al. Noninvasive imaging of the thirteen-lined ground squirrel photoreceptor mosaic. *Vis Neurosci*. 2016;33: e003.

33. Geng Y, Dubra A, Yin L, et al. Adaptive optics retinal imaging in the living mouse eye. *Biomed Opt Express*. 2012;3:715–734.

34. Schallek J, Geng Y, Nguyen H, Williams DR. Morphology and topography of retinal pericytes in the living mouse retina using in vivo adaptive optics imaging and ex vivo characterization. *Invest Ophthalmol Vis Sci*. 2013;54:8237–8250.

35. Geng Y, Greenberg KP, Wolfe R, et al. In vivo imaging of microscopic structures in the rat retina. *Invest Ophthalmol Vis Sci*. 2009;50:5872–5879.

36. Rosolen SG, Lamory B, Harms F, Sahel JA, Picaud S, LeGargasson JF. Cellular-resolution in vivo imaging of the feline retina using adaptive optics: Preliminary results. *Vet Ophthalmol*. 2010; 13:369–376.

37. Headington K, Choi SS, Nickla D, Doble N. Single cell imaging of the chick retina with adaptive optics. *Curr Eye Res*. 2011;36:947–957.

38. Hunter JJ, Masella B, Dubra A, et al. Images of photoreceptors in living primate eyes using adaptive optics two-photon ophthalmoscopy. *Biomed Opt Express*. 2010;2:139–148.

39. Ross JW, Fernandez de Castro JP, Zhao J, et al. Generation of an inbred miniature pig model of retinitis pigmentosa. *Invest Ophthalmol Vis Sci*. 2012;53:501–507.

40. Sulai YN, Dubra A. Optical design of broadband scanning adaptive optics ophthalmoscope for the mouse eye. In: Bifano TG, Kubby J, Gigan S, eds. *MEMS Adaptive Optics VIII*. San Francisco, CA: Proceedings SPIE; 2014.

41. Scoles D, Sulai YN, Langlo CS, et al. In vivo imaging of human cone photoreceptor inner segments. *Invest Ophthalmol Vis Sci*. 2014;55: 4244–4251.

42. Scoles D, Sulai YN, Dubra A. In vivo dark-field imaging of the retinal pigment epithelium cell mosaic. *Biomed Opt Express*. 2013;4:1710–1723.

43. Salmon AE, Cooper RF, Langlo CS, Baghaie A, Dubra A, Carroll J. An automated reference frame selection (ARFS) algorithm for cone imaging with adaptive optics scanning light ophthalmoscopy. *Transl Vis Sci Technol*. 2017;6:9.

44. Dubra A, Harvey Z. Registration of 2D images from fast scanning ophthalmic instruments. In: Fischer B, Dawant B, Lorenz C, eds. *Biomedical Image Registration*. Berlin: Springer-Verlag; 2010: 60–71.

45. Cunefare D, Cooper RF, Higgins B, et al. Automatic detection of cone photoreceptors in split detector adaptive optics scanning light ophthalmoscope images. *Biomed Opt Express*. 2016;7:2036–2050.

46. Schneider CA, Rasband WS, Eliceiri KW. NIH Image to ImageJ: 25 years of image analysis. *Nat Methods*. 2012;9:671–675.

47. Thévenaz P, Ruttimann UE, Unser M. A pyramid approach to subpixel registration based on intensity. *IEEE Trans Image Process*. 1998;7: 27–41.

48. Chiu SJ, Li XT, Nicholas P, Toth CA, Izatt JA, Farsiu S. Automatic segmentation of seven retinal layers in SDOCT images congruent with expert manual segmentation. *Opt Express*. 2010; 18:19413–19428.

49. Wilk MA, Huckenpahler AL, Collery RF, Link BA, Carroll J. The effect of retinal melanin on optical coherence tomography images. *Transl Vis Sci Technol*. 2017;6:8.

50. Sajdak BS, Bell BA, Lewis TR, et al. Assessment of outer retinal remodeling in the hibernating 13-lined ground squirrel. *Invest Ophthalmol Vis Sci*. 2018;59:2538–2547.

51. Cooper RF, Wilk MA, Tarima S, Carroll J. Evaluating descriptive metrics of the human cone mosaic. *Invest Ophthalmol Vis Sci*. 2016;57:2992–3001.

52. Staurenghi G, Sadda S, Chakravarthy U, Spaide RF, Panel IO. Proposed lexicon for anatomic landmarks in normal posterior segment spectral-domain optical coherence tomography: the IN•OCT consensus. *Ophthalmology*. 2014;121: 1572–1578.

53. Scott PA, de Castro JP, DeMarco PJ, et al. Progression of Pro23His retinopathy in a miniature swine model of retinitis pigmentosa. *Transl Vis Sci Technol*. 2017;6: eCollection.

translational vision science & technology

54. Dees EW, Dubra A, Baraas RC. Variability in parafoveal cone mosaic in normal trichromatic individuals. *Biomed Opt Express*. 2011;2:1351–1358.

55. Xie W, Zhao M, Tsai SH, et al. Data on SD-OCT image acquisition, ultrastructural features, and horizontal tissue shrinkage in the porcine retina. *Data Brief*. 2018;21:1019–1025.

56. Xie W, Zhao M, Tsai SH, et al. Correlation of spectral domain optical coherence tomography with histology and electron microscopy in the porcine retina. *Exp Eye Res* 2018;177:181–190.

57. Stein DM, Wollstein G, Ishikawa H, Hertzmark E, Noecker RJ, Schuman JS. Effect of corneal drying on optical coherence tomography. *Ophthalmology*. 2007;113:985–991.

58. Bell BA, Kaul C, Hollyfield JG. A protective eye shield for prevention of media opacities during small animal ocular imaging. *Exp Eye Res*. 2014;127:280–287.

59. Scott PA, Fernandez de Castro JP, Kaplan HJ, McCall MA. A Pro23His mutation alters prenatal rod photoreceptor morphology in a transgenic swine model of retinitis pigmentosa. *Invest Ophthalmol Vis Sci*. 2014;55:2452–2459.

60. Wang W, Lee SJ, Scott PA, et al. Two-step reactivation of dormant cones in retinitis pigmentosa. *Cell Rep*. 2016;15:372–385.

61. Curcio CA, Packer O, Kalina RE. A whole mount method for sequential analysis of photoreceptor and ganglion cell topography in a single retina. *Vision Res*. 1987;27:9–15.

62. Garrioch R, Langlo C, Dubis AM, Cooper RF, Dubra A, Carroll J. Repeatability of in vivo parafoveal cone density and spacing measurements. *Optom Vis Sci*. 2012;89:632–643.

63. Abozaid MA, Langlo CS, Dubis AM, Michaelides M, Tarima S, Reliability Carroll J. and repeatability of cone density measurements in patients with congenital achromatopsia. *Adv Exp Med Biol*. 2016;854:277–283.

64. Zayit-Soudry S, Sippl-Swezey N, Porco T, et al. Repeatability of cone spacing measures in eye with inherited retinal degenerations. *Invest Ophthalmol Vis Sci*. 2015;56:6179–6189.

65. Tanna P, Kasilian M, Strauss R, et al. Reliability and repeatability of cone density measurements in patients with Stargardt disease and RPGR-associated retinopathy. *Invest Ophthalmol Vis Sci*. 2017;58:3608–3615.

66. Fernandez de Castro JP, Scott PA, Fransen JW, et al. Cone photoreceptors develop normally in the absence of functional rod photoreceptors in a transgenic swine model of retinitis pigmentosa. *Invest Ophthalmol Vis Sci*. 2014;55:2460–2468.

translational vision science & technology